A transition mass for black holes to show broad emission lines

Susmita Chakravorty[1,2] Martin Elvis[2*], Gary Ferland[3*]

[1]*Harvard University, Department of Astronomy, schakravorty@head.cfa.harvard.edu;*
[2]*Harvard-Smithsonian Center for Astrophysics, 60 Garden Street, Cambridge, MA 02138, USA*
[3]*Department of Physics and Astronomy, University of Kentucky, Lexington, KY 40506.*

15 November 2012

ABSTRACT

Although the super-massive (AGN) and stellar mass (XRBs) black holes have many properties in common, the broad emission lines (BELs) are exclusively signatures of the AGN. Based on the detection of these lines from SDSS data bases, there seems to be no AGN with mass $M_{BH} \lesssim 10^5 M_\odot$. In this paper we investigate if such low mass black holes are really non-existent or they are undetected because the BELs in them are not produced efficiently. Using the ionizing spectral energy distribution for a wide range of black hole mass, $10 - 10^9 M_\odot$, spanning XRBs to AGN, we calculate the equivalent widths (EWs) of ultraviolet and optical lines Lyα 1216 Å, Hβ 4861 Å, CIV 1549 Å and MgII 2798 Å. The LOC (locally optimally emitting cloud) model has been used to describe the broad emission line region (BELR) for the calculations. We find that the hardening of the SED shape with decreasing mass do not decrease the BEL EWs. However, finite size of the BELR, as measured by the line widths, which is controlled by the mass of the black hole, regulates the production of these emission lines. There seems to be a peak in the EWs of the emission lines for typical AGN black holes of $\sim 10^8 M_\odot$, below which the lines become intrinsically fainter with a sharp fall-off below $\sim 10^6 M_\odot$. This may be the cause of the absence of low mass AGN in SDSS.

Key words: Galaxies - quasars: emission lines, galaxies: active, Seyfert, Physical Data and Processes - accretion, accretion discs, black hole physics, line: formation

1 INTRODUCTION

Active galactic nuclei (AGN) and X-ray binaries (XRBs) share many properties, but broad emission lines (BELs) are not among them. The absence of BELs in XRB spectra are often ascribed to the harder spectrum that is emitted by the accretion disk around the $\lesssim 10^6$ times smaller black holes. Here we investigate the predicted BEL equivalent widths (EWs) over a wide range of black hole masses, $10 - 10^9 M_\odot$ to see if there is a threshold mass below which BELs are not expected. The possibility of a threshold mass for strong BEL production has become interesting from recent observational results, which seem to suggest that there are no broad line emitting black holes below $M_{BH} \lesssim 10^5 M_\odot$ (Greene & Ho 2004). Is this because there are no such black holes, or is it that, even when accreting at substantial rates, such black holes cannot produce BELs with detectable EWs?

Most existing photoionization calculations for the broad emission lines in AGN, study the line strengths as a function of the overall shape of the ionizing continuum (Osterbrock & Ferland 2006; Leighly & Casebeer 2007) and the luminosity of the AGN. However, mostly, these studies do not take the further step of directly relating the emission line properties to M_{BH} and $\dot{m}$. On the other hand, dynamical measurements of M_{BH}, from the widths of the broad lines, and/or using the reverberation mapping techniques, (Peterson 1993; Netzer & Peterson 1997; Kaspi et.al. 2000) con-

sider an average $R_{BELR} \sim L_{AGN}^{1/2}$ relationship and do not need to delve into the details of the line strengths and ratios. In this study we shall use the LOC model, where the broad lines are due to locally, optimally emitting clouds, first suggested by Baldwin et.al. (1995). We calculate the line strengths of the strongest broad lines, Lyα 1216 Å, Hβ 4861 Å, CIV 1549 Å and MgII 2798 Å, as a function of the black hole mass ranging from $10 - 10^9 M_\odot$.

2 THEORY

2.1 The accretion disk spectral energy distribution

The radiation from the thin accretion disc (α-disk) may be modeled as a sum of local blackbodies emitted from the different annuli of the disc at different radii (Shakura & Sunyaev 1973, hereafter SS73). The temperature of the annulus at radius R is

$$T(R) = 6.3 \times 10^5 \left(\frac{\dot{m}}{\dot{m}_{\rm Edd}} \right)^{\frac{1}{4}} \left(\frac{M_{BH}}{10^8 M_\odot} \right)^{-\frac{1}{4}} \left(\frac{R}{R_s} \right)^{-\frac{3}{4}} \text{K} \quad (1)$$

(Peterson 1997; Frank et al. 2002) where $\dot{m}$ is the accretion rate of the central black hole of mass M_{BH}, $\dot{m}_{\rm Edd}$ is its Eddington accretion rate and $R_s = 2GM_{BH}/c^2$ is the Schwarzschild radius (G is the gravitational constant and c is the velocity light). The normalisation constant A_{dbb} for this spectral component is given by
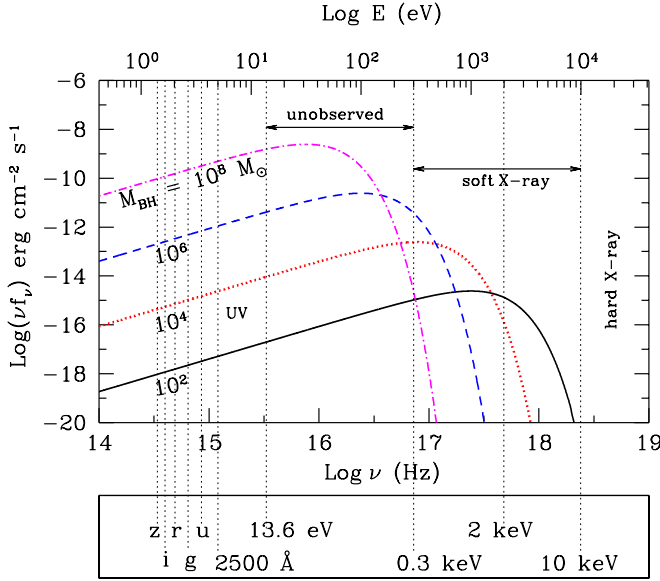
Log E (eV)

Figure 1. The spectral energy distribution from accretion disks around black holes of mass $M_{BH} = 10^2, 10^4, 10^6$ and 10^8 M$_\odot$ accreting at $0.1\dot{m}_{\rm Edd}$ (or emitting at $0.1L_{\rm Edd}$). The absolute scale of the y axis is arbitrary, assuming that all the sources are at a distance of 100 Mpc. However, the relative normalisations of the SEDs are according to their mass ratios. We have labeled some of the important energy values (accompanied by the dotted vertical lines) relevant for AGN SEDs. In particular, note the positions of the u (3551 Å), g(4686 Å), r(6165 Å), i(7481 Å) and z(8931 Å) filters used by the Sloan Digital Sky Survey.

$$A_{dbb} = \left\{ \frac{R_{in}/{\rm km}}{D/(10\ {\rm kpc})} \right\}^2 \cos\theta \qquad (2)$$

for an observer at a distance D whose line-of-sight makes and angle θ to the normal to the disc plane. R_{in} is the radial distance of the innermost stable annulus of the accretion disc from the black hole. R_{in} is assumed to be a 3 R_s (as conventional).

A standard model for the spectral component from the accretion disk is available as disk blackbody (Mitsuda et al. 1984; Makishima et al. 1987) in XSPEC[1] (Arnaud 1996). We have used version 11.3 of XSPEC to generate the *disk blackbody* spectral component $f_{dbb}(\nu)$ for $M_{BH} = 10 - 10^9 M_\odot$ at steps of $\log(M_{BH}/M_\odot) = 0.5$ and $\dot{m} = 0.1\dot{m}_{\rm Edd}$ and $\theta = 30°$ are held constant. The spectral energy distributions (SEDs) for $M_{BH} = 10^2, 10^4, 10^6$ and 10^8 M$_\odot$ are shown in Figure 1 to demonstrate how the peak of the SED and its normalisation change as a function of the black hole mass. The SEDs for AGN with $M_{BH} \geq 10^4 M_\odot$ peak in an energy range which is unobservable for extragalactic sources due to Galactic extinction. As a result, for AGN, determination of the mass of the black hole often depends on the study of the emission lines, particularly the BELs (Netzer 1987; Korista et.al. 1997b; Kaspi et.al. 2000; Bentz et al. 2006).

AGN are often selected from large databases like Sloan Digital Sky Survey (hereafter SDSS) based on their broadband optical colours, which depend on the intrinsic SED of the AGN. From Figure 1 we see that all of the five SDSS filters (u-3551, g-4686, r-6165, i-7481 and z-8931 Å) are positioned on the linear, same slope 'low energy' tail of the intrinsic AGN SEDs so that they cannot be

distinguished as black holes of different mass, merely from studying the SDSS colours. SDSS, however observes the redshifted and not the intrinsic SEDs of the quasars. Even when seeing the redshifted SED, there is no effect of the mass on the SDSS colors for $z < 8.60$ for $M_{BH} \leq 10^6 M_\odot$

Even if the colour selection algorithms of SDSS are not biased against detecting the lower mass black holes, they will still drop out because the intrinsic luminosity of the AGN decreases with the mass of the black hole. For example, based on the flux limits of the SDSS filters (Stoughton et al. 2002), the $M_{BH} = 10^6 M_\odot$ black holes drop out beyond a redshift $z \geq 0.075$, whereas a $M_{BH} = 10^8 M_\odot$ black hole can be seen for $z \leq 1.25$. Note that the aforementioned redshift limits are based on the continuum flux only. AGN are however detected primarily through the detection of their emission lines. The limits based on the emission lines would be different and we shall discuss this further in Section 3.

2.2 The LOC model for the BELR

Baldwin et.al. (1995) and Korista et.al. (1997a) show that, for a given SED, any particular emission line is dominated by emission from a fairly narrow range of gas density (n_H) and incident flux $\Phi(H)$ [= $Q(H)/4\pi R^2$, where $Q(H)$ is the number of hydrogen ionizing photons and R is the distance of the cloud from the source of the ionizing radiation]. This narrow range of the n_H and $\Phi(H)$ is different for different emission lines. However, as long as there are enough clouds distributed over the relevant density and distance ranges, all the observed emission lines can be formed with the observed line ratios. This is thus, a model, which does not require any extreme fine tuning of n_H and $\Phi(H)$ to produce all the observed emission lines. Leighly & Casebeer (2007) discuss both the successes and limitations of the LOC model. Among limitations they mention that (a) some of the parameters of the model like the indices of the density and radial distribution of the clouds cannot be physically interpreted and (b) the model does not include some physical effects like self-shielding.

3 CALCULATIONS

3.1 Unrestricted BELR

For each model SED we use version C08.00 of CLOUDY[2](Ferland et.al. 1998). to calculate the emission line spectrum for a three dimensional parameter grid of $\Phi(H)$, n_H and column density (N_H). $\log \Phi(H)$ is varied from 17–24 in steps of 0.5, $\log n_H$ from 7–14 in steps of 0.5 and $\log N_H$ from 21–23 in steps of 0.5, assuming a Solar metallicity (Allende Prieto et al. 2001, 2002; Holweger 2001; Grevesse & Sauval 1998) gas. We calculate the equivalent widths (EWs) of the 42 more prominent quasar emission lines (see Korista et.al. 1997a, for the entire list). However, we demonstrate the results for only four of the strongest lines (Lyα 1216 Å, CIV 1549 Å, MgII 2798 Å and Hβ 4861 Å) in this paper, which is adequate for the issues discussed here.

We plot the iso-contours of the predicted EW (in log) for the 1549 Å CIV line in the $\log n_H - \log \Phi(H)$ plane (Figure 2) for the four SEDs with $M_{BH} = 10^{2.0}, 10^{4.0}, 10^{6.0}$, and $10^{8.0}$M$_\odot$. In the $\log \Phi(H) - \log n_H$ plane, diagonal lines with a slope of 45° are lines of constant ionization parameter $U = \Phi(H)/cn_H$, where the value of U increases from the bottom right to the top left. We see

[1] http://heasarc.gsfc.nasa.gov/docs/xanadu/xspec/
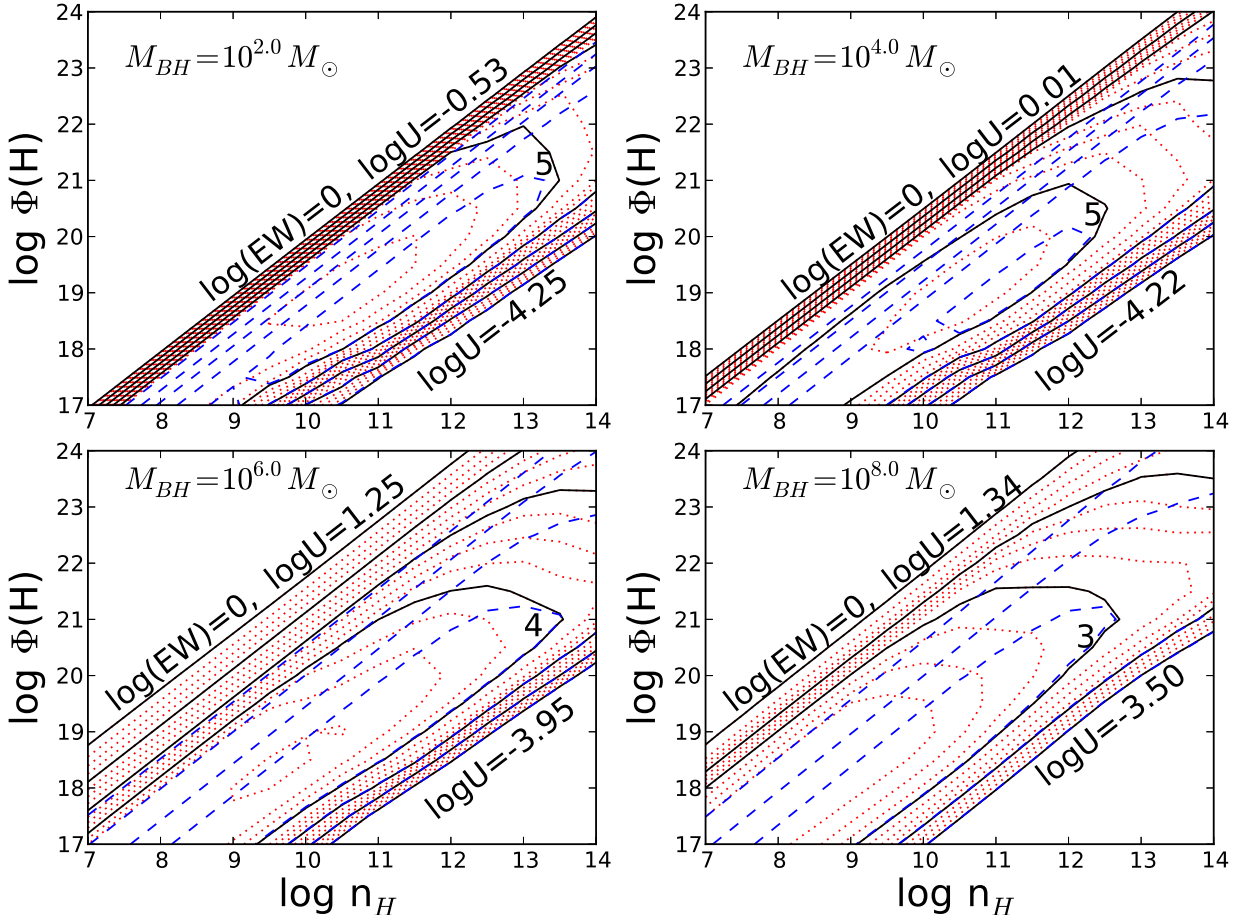
[2] URL: http://www.nublado.org/

Figure 2. Contour plots for the CIV (1549 Å) equivalent width as a function of the black hole mass in the $n_H - \Phi(H)$ plane. The bold solid black lines are contours at steps of 1 dex and the intermediate dotted red lines are contours at steps of 0.25 dex, for $\log N_H = 23$. In each panel, the outermost contours correspond to EW = 1 ($\log(EW) = 0$), whereas the innermost contours of the maximum EW are different for different SEDs. Note that diagonal lines with a slope of 45° in the $\log \Phi(H) - \log n_H$ plane are lines of constant ionization parameter $U = \Phi(H)/cn_H$. In each panel, we have labeled the value of $\log U$ corresponding to the outermost EW = 1 contour, both at the low ionization and high ionization end. For comparison, we also over plot the iso-contours for $\log N_H = 21$ (dashed blue lines) at steps of 1 dex, the outermost contour being for $\log(EW) = 0$.

that the contours form well-defined diagonal ridges (collection of constant U lines) in the $\log \Phi(H) - \log n_H$ plane with significant EW (> 1). In each panel of Figure 2 we have also labeled the limiting values of $\log U$, within which CIV line is efficiently produced with $1 \leq EW \leq 10^{5.75}$ for $M_{BH} = 10^{2.0} M_\odot$, $1 \leq EW \leq 10^{5.25}$ for $M_{BH} = 10^{4.0} M_\odot$, $1 \leq EW \leq 10^{4.75}$ for $M_{BH} = 10^{6.0} M_\odot$, and $1 \leq EW \leq 10^{3.75}$ for $M_{BH} = 10^{8.0} M_\odot$.

Deviations (of any contour) from the 45° lines show where thermal heating of the gas begins to be more important than photoionization, usually at high n_H and high $\Phi(H)$ (upper right, each panel). For example, taking the example of the $\log(EW) = 4$ contour for $M_{BH} = 10^{2.0} M_\odot$, we see that it 'turns over' from high $\log U (= -0.99, \log n_H \geq 12$ and $\log \Phi(H) \geq 21.5)$ and becomes diagonal again at a lower $\log U (= -3.24)$.

The contours for $\log N_H = 21$ and 23, show that the low ionization ridge (lower-right) of the iso-contours remain unaffected. However, the high ionization ridge (upper-left) is pushed to lower U, e.g by 1.23 dex for the $M_{BH} = 10^{8.0} M_\odot$ SED. Thus for any given SED, lower column density restricts efficient line production to a tighter range of U.

To assess the contribution from all the clouds of different den-

sity and column density and at different distances, we have to take a weighted average of EW :

$$\mathcal{EW} = f \int \int \int EW(\Phi(H), n_H, N_H) \frac{d \Phi(H)}{\Phi(H)} \frac{d n_H}{n_H} \frac{d N_H}{N_H} \quad (3)$$

over $21 \leq \log N_H \leq 23$, $8 \leq \log n_H \leq 14$ and $18 \leq \log \Phi(H) \leq 24$ all in steps of 0.5. $f = 0.2$ is the constant covering fraction adopted in this paper. $\mathcal{EW}$ (in log) as a function of M_{BH} for Lyα, CIV, MgII and Hβ is shown in Figure 3 (dotted black line). For each of the emission lines, the average $\mathcal{EW}$ rises monotonically with the decrease in mass.

We further calculate the line ratios MgII/CIV and MgII/Hβ and plot them against each other in Figure 4 (dotted black line). The labeled solid black circles along the line mark the black hole masses in units of $\log(M_{BH}/M_\odot)$.

3.2 Restriction on the radius of the BELR

3.2.1 Limits from velocity of the clouds

Reverberation mapping has established that the time lag between the variation in the continuum flux and the line flux t_{lag} is propor-
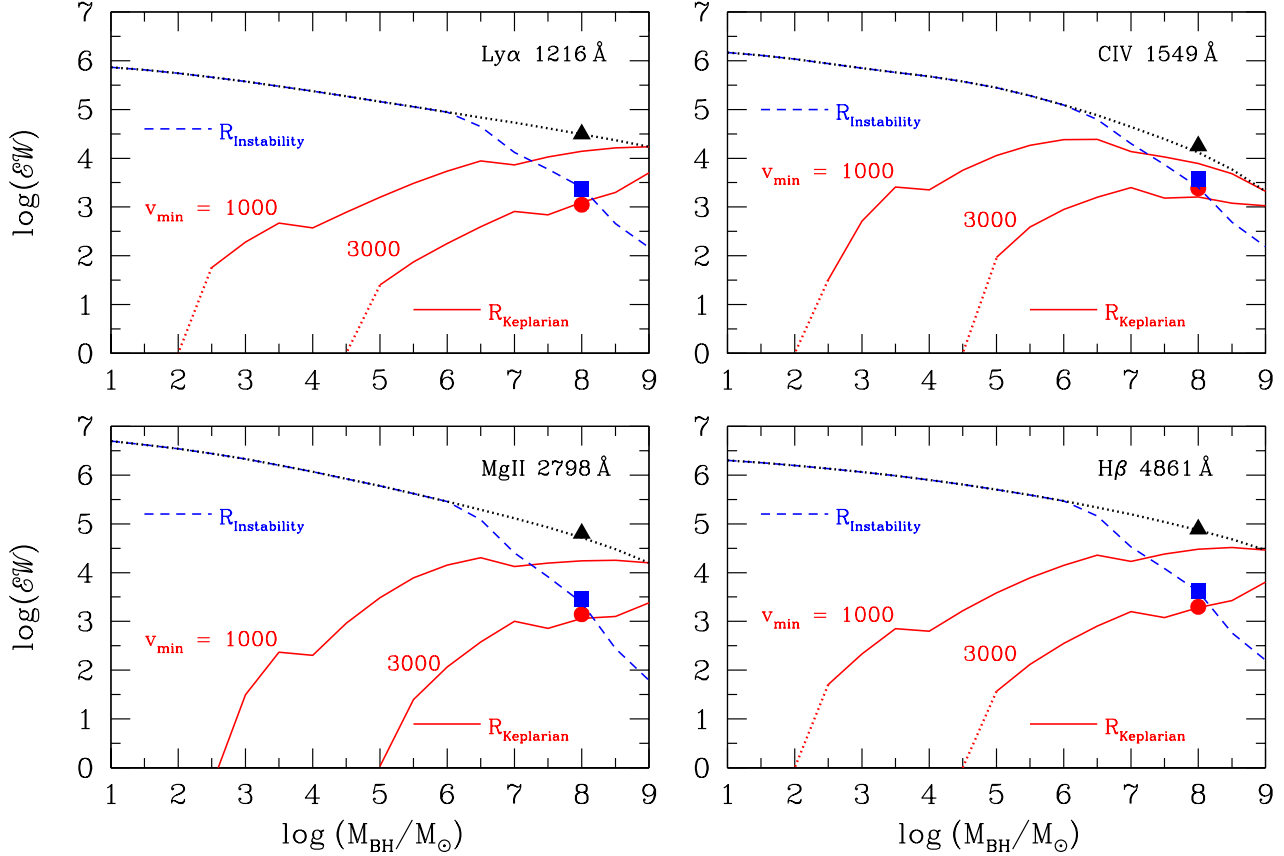
Figure 3. The weighted average ($\mathcal{EW}$) for four of the strongest broad lines, as a function of black hole mass is given by the dotted black line in each panel. The filled black triangle at $M_{BH} = 10^{8.0} M_{\odot}$ shows the value of $\mathcal{EW}$ if we consider an SED with a disk blackbody plus a X-ray power-law, instead of just a disk blackbody SED. The mass distribution of $\mathcal{EW}$ is modified if a cut-off is applied on the maximum allowed radius of the BELR; the solid red curves (with different minimum velocity of the BELR clouds, in $\mathrm{km\,s^{-1}}$) if the cut-off is determined using Keplerian mechanics (Equation 4) and the dashed blue curve if the cut-off is determined from the considerations of the gravitational instability radius of the accretion disk (Equation 5). The filled red circle and the filled blue square denote the value of $\mathcal{EW}$ for the disk+power-law SED for $M_{BH} = 10^{8.0} M_{\odot}$ when the respective radius cut-off schemes (as described above) are assumed. Note that for the Keplerian cut-off mechanism, we have shown the filled circle only for the $v_{min} = 3000 \,\mathrm{km\,s^{-1}}$ case.

tional to 1/2 power of the full width at half maxima (FWHM, see Bentz et al. 2006, and references therein). Hence the BELR gas seems to move with Keplerian or at least virialized velocities, so that we can define the outermost radius of the BELR

$$R_{Keplerian} = G\,M_{BH}/v_{min}^2 \qquad (4)$$

corresponding to the clouds with the lowest observed velocity v_{min}. The FWHM of BEL are $\gtrsim 2000(> 1200)\,\mathrm{km\,s^{-1}}$ (Hao et al. 2005), so that $v_{min}(= \mathrm{FWHM}/\sqrt{8\ln2}) \gtrsim 1000\,\mathrm{km\,s^{-1}}$. The distribution of $R_{Keplerian}$ are shown as solid red lines in Figure 5, for $v_{min} = 1000, 3000$ and $10000\,\mathrm{km\,s^{-1}}$.

Introducing an $R_{Keplerian}$ cut-off in our CLOUDY simulations, produces a pronounced cut-off in $\mathcal{EW}$ (solid red lines in Figure 3). BELs used by SDSS to detect and identify AGN activity, Hβ 4861 Å, CIV 1549 Å and MgII 2798 Å are all affected. The ratio $\mathcal{EW}_{7.5}/\mathcal{EW}_{5.0} > 10$ for all the emission lines, for $v_{min} = 3000\,\mathrm{km\,s^{-1}}$ (Table 1), where $\mathcal{EW}_x$ is the $\mathcal{EW}$ due to the black hole mass $M_{BH} = 10^x M_{\odot}$. This ratio is as high as 720 for MgII 2798 Å. Below $M_{BH} = 10^{5.0} M_{\odot}$, $\mathcal{EW}$ rapidly falls for all the lines.

The larger BELR allowed by $v_{min} = 1000\,\mathrm{km\,s^{-1}}$ produces a less drastic drop and theory predicts non-zero equivalent widths

Cut-off used (v_{min} km/s)	CIV − 1549Å		MgII − 2798Å		Hβ − 4861Å	
	$\dfrac{\mathcal{EW}_{7.5}}{\mathcal{EW}_{4.0}}$	$\dfrac{\mathcal{EW}_{7.5}}{\mathcal{EW}_{5.0}}$	$\dfrac{\mathcal{EW}_{7.5}}{\mathcal{EW}_{4.0}}$	$\dfrac{\mathcal{EW}_{7.5}}{\mathcal{EW}_{5.0}}$	$\dfrac{\mathcal{EW}_{7.5}}{\mathcal{EW}_{4.0}}$	$\dfrac{\mathcal{EW}_{7.5}}{\mathcal{EW}_{5.0}}$
3000	-	17.52	-	720	-	32.22
1000	4.83	0.96	79.31	5.27	39.37	6.27

Table 1. The ratio of the weighted equivalent widths $\mathcal{EW}$ for different black hole masses. We have considered the finite size of the BELR, cut-off corresponding to the two Keplerian velocities $v_{min} = 3000$ and $1000\,\mathrm{km\,s^{-1}}$.

upto much lower black hole masses ($\sim 10^{2.5} M_{\odot}$). For $v_{min} = 1000\,\mathrm{km\,s^{-1}}$, $\mathcal{EW}_{7.5}/\mathcal{EW}_{5.0}$ reduces to 5.27 for MgII 2798 Å. Table 1 list the equivalent width ratios for the different lines. In fact for the two CIV and MgII lines the $\mathcal{EW}$ profiles are not monotonically decreasing functions of black hole mass, rather the peak of the profiles shift to lower mass $\sim 10^{6.5} M_{\odot}$.
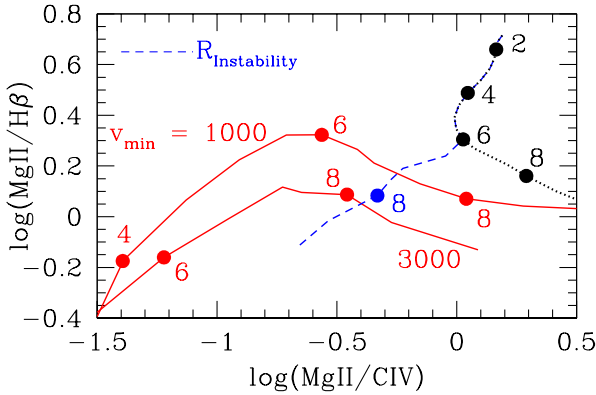
Figure 4. The line ratios $MgII/CIV$ and $MgII/H\beta$ are plotted against each other for the three different BELR. The case of Unrestricted BELR (Section 3.1), with no upper limits on its size, is represented by the dotted black line. When the BELR is truncated using limits from observed Keplerian velocities (Section 3.2) we have line ratio profiles given by the solid red lines, for the two different velocities of the clouds, namely, $v_{min} = 1000$ and $3000\,\mathrm{km\,s^{-1}}$. The dashed blue line corresponds to BELR with size limitations imposed by the gravitational instability (Section 3.2.2). The solid circles represent the points on the line ratio profiles for different black hole masses (as labeled) in units of $\log(M_{BH}/M_\odot)$.

The detection of the lines by SDSS would however, depend on the intrinsic luminosity in the emission lines, in addition to their equivalent widths. The intrinsic luminosity in the lines, in turn depend on the mass of the black hole. When no limit is imposed on the outer radius of the BELR, our calculations indicate that using the SDSS filters, the $MgII$ 2798 Å line should be detected upto a redshift of 0.67 and the $H\beta$ 4861 Å line upto 0.27 for a $10^6 M_\odot$ black hole. This is not what is observed. On the other hand, when limits on the size of the BELR are imposed, a $10^6 M_\odot$ black hole cannot be detected (for both $v_{min} = 1000$ and $\mathrm{km\,s^{-1}}$) using either of $MgII$ 2798 Å or $H\beta$ 4861 Å lines, a situation more in line with the observations.

The line ratios $MgII/H\beta$ vs $MgII/CIV$, for the size limited BELR, using Keplerian cut-offs, are plotted using the solid red lines in Figure 4. The profiles are very different from the case of the unrestricted BELR (dotted black lines). For a $10^8 M_\odot$, the values for $MgII/H\beta$ are almost same for the size limited and the unrestricted BELR, but the line ratio $MgII/CIV$ is very different in the two cases. This line ratio varies from the unrestricted BELR case by 0.25 dex for $v_{min} = 1000\,\mathrm{km\,s^{-1}}$ and by 0.74 dex for $v_{min} = 3000\,\mathrm{km\,s^{-1}}$. For a $10^6 M_\odot$, black, even the $MgII/H\beta$ ratio varies from the unrestricted BELR case by 0.47 dex in the $v_{min} = 3000\,\mathrm{km\,s^{-1}}$ limited BELR. The $MgII/CIV$ line ratio varies from the unrestricted BELR case by 0.59 dex for $v_{min} = 1000\,\mathrm{km\,s^{-1}}$ and by 1.24 dex for $v_{min} = 3000\,\mathrm{km\,s^{-1}}$. Such variations in the line ratios for different physical scenarios of the BELR, would act as diagnostics in our future publications when we shall compare our theoretical results with observations from SDSS or the likes of it, not only for these three emission lines, but for many more appropriately chosen broad emission lines.

3.2.2 Gravitational disk instability

The outer parts of the α-disk becomes self-gravitating and breaks up. This radius has been suggested as the outer boundary of the BELR and the beginning of the "torus" (Suganuma et al.
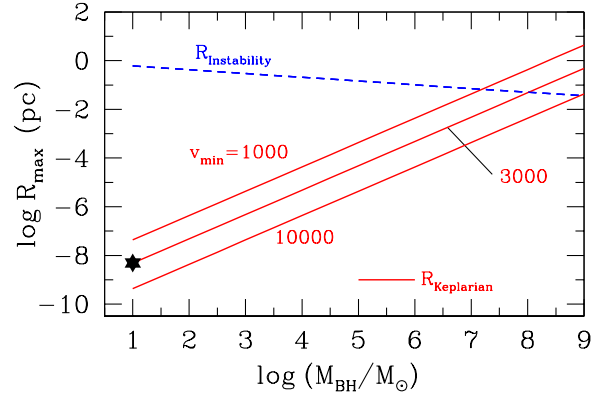
Figure 5. The outer radius of BELR as a function of black hole mass. Various methods of determining this cut-off radius are demonstrated : considering (a) a phenomenological approach based on the observed velocities of the emission lines (solid red lines) and (b) gravitational instability of the accretion disk (dashed blue line). For stellar mass black hole ($M_{BH} = 10 M_\odot$), the black star shows the tidal disruption radius.

2006; Netzer & Laor 1993). The radius at which the disk becomes Toomre unstable (the Toomre parameter $Q < 1$ Binney & Tremaine 1987) depends weekly on the central black hole mass. Translating the Toomre criterion in terms of the α-disk parameters, $\Sigma/H = M_{BH}/R_{Instability}^3$, ($\Sigma$ is the surface density and H is the scale height of the disk) gives us

$$R_{Instability}^{-\frac{9}{8}} = 1.31 \times 10^2 1 \alpha_{disk} \left(\frac{\dot{m}}{\dot{m}_{Edd}}\right)^{\frac{11}{20}} \left(\frac{M_{BH}}{M_\odot}\right)^{\frac{7}{40}} f^{\frac{11}{5}} \quad (5)$$

where $f^4 = 1 - \left(\frac{6GM_{BH}}{M_\odot}\right)^{\frac{1}{2}}$. The much weaker mass evolution of $R_{Instability}$ (compared to $R_{Keplerian}$) is shown as a dashed blue line in Figure 5.

Using the $R_{Instability}$ cut off, below $M_{BH} \sim 10^{6.0} M_\odot$, the $\mathcal{EW}$ distribution is same as when no radius restriction is applied, leading to the unobserved increase in $\mathcal{EW}$ with decreasing mass (dashed blue curves in Figure 3). The line corresponding line ratios $MgII/H\beta$ vs $MgII/CIV$ are shown by the dashed blue line in Figure 4, further showing that the line fluxes are exactly the same as that for an unrestricted BELR for $M_{BH} <= 10^{6.0} M_\odot$

3.2.3 Tidal disruption by stellar mass black holes

According to Hills (1975); Gezari et al. (2003),

$$R_{Tidal} = 1.1 R_{sch} \left(M_{BH}/10^8 M_\odot\right)^{-2/3}, \quad (6)$$

for solar mass disrupted stars. Thus the disruption does not happen for $M_{BH} > 1.1 \times 10^8 M_\odot$ – the stars are swallowed whole. Thus we use Equation 6 to calculate R_{Tidal} for a black hole of $M_{BH} = 10 M_\odot$ having a solar mass binary companion. The tidal disruption is plotted as a black star in Figure 5 and we find that $R_{Tidal} \sim R_{Keplerian}$ for $v_{min} = 3000$. Our calculations for $\mathcal{EW}$ suggest zero flux in the emission lines for such low mass black holes (see Figure 3) when the BELR size limit is imposed with $v_{min} = 3000\,\mathrm{km\,s^{-1}}$. No high sensitivity search for these emission lines have been conducted for stellar mass black holes to corroborate or contradict these theoretical results.

4   DISCUSSION AND FUTURE WORK

• Additional components of the AGN SED :
Both the AGN (super-massive black holes) and the XRBs (solar mass black holes) are powered by the active matter accretion into the black hole. However, the emission from the accretion disk is not the only component of the observed SED from the AGN or the XRBs. In both cases we also observe power-law emission at higher energies ($\geq 500\,\mathrm{eV}$ for AGN and $\geq 3\,\mathrm{keV}$ for XRBs). The power-law is thought to be due to inverse comptonisation of some of the disk photons by the hot coronal plasma surrounding the black hole, or due to the jet (particularly for XRBs). In case of AGN of type 1, sometimes we see an additional component, the soft-excess at $< 1\,\mathrm{keV}$, which may be comptonized disk emission or an entirely separate component altogether. Often the soft excess can be modeled as a blackbody of temperature $100 - 200\,\mathrm{keV}$. However, for all the calculations presented in this paper, we ignore the power-law and the soft-excess components of the SED, because their shape or strength are independent of the mass of the black hole.

The strengths of the lines are determined by the available number of photons close to the ionization potential (IP) of the relevant ions. In this paper we have restricted our studies to black holes with $M_{BH} \lesssim 10^9 M_\odot$ because it was sufficient to consider only the mass dependent accretion disk component of the SED. In this mass range, the accretion disk is hot enough that the energy ranges of the ionization or excitation potentials ($\lesssim 50\,\mathrm{eV}$) required to produce the lines Hβ 4861 Å, CIV 1549 Å and MgII 2798 Å are dominated by the disk emission and the power-law or the soft excess would contribute less than 1% of the radiation from the accretion disk.

To be thorough, we investigated the effect of adding a X-ray power-law with spectral index $\alpha = 0.8$ and $\alpha_{OX} = 1.2$ for $M_{BH} = 10^{8.0} M_\odot$. In each panel of Figure 3, the resultant $\mathcal{EW}$s are shown as filled black triangles, for an unrestricted BELR, as filled red circle for the $v_{min} = 3000\,\mathrm{km\,s^{-1}}$ Keplerian limit on the BELR and as filled blue squares for the BELR restricted by gravitational instability. In each case these points lie exactly on the line for the $\mathcal{EW}$ distribution, generated using only the accretion disk component, showing that the addition of the power-law and the soft-excess component is redundant for these emission lines in the black hole mass range considered.

However, while considering similar studies for higher mass black holes, one has to carefully account for the other aforementioned components of the AGN SED because, the high energy tail of the accretion disk SED for $M_{BH} >= 10^9 M_\odot$ may cut-off at less than $50\,\mathrm{eV}$.

Similar considerations are required for constructing the AGN SED required to correctly predict the $\mathcal{EW}$ for OVI 1034 Å, which is an important BEL in the UV. The IP of OV is 113.90 eV, an energy range dominated by the power-law for quasar-like ($M_{BH} \gtrsim 10^{8.0} M_\odot$) SED. Thus $\mathcal{EW}$ calculations for OVI would require an AGN SED including all the components, and not just the accretion disk emission. We will study such emission lines in details in our future publications.

• Alternative models for the accretion disk :
Instead of a radiatively efficient thin accretion disk (BBB, due to Shakura & Sunyaev 1973, , SS73), sometimes black holes might have advection dominated, radiatively inefficient accretion flows, which would result in significantly different SEDs (see e.g. Hopkins et.sl. 2009) that the SS73 models (considered in this paper). These alternative prescriptions drastically change the shape of the SED in the energy range of the IP of the ions responsible for the BELs and the narrow emission lines (NELs). We intend to calculate the line strengths due to such ionizing SEDs and predict observable signatures, which might act as diagnostic tools.

Even for the BBB, more rigorous models exist for modeling the radiation from the accretion disk (BBB). For example, Blaes et al. (2001); Hubeny et al. (2000, 2001); Hui et al. (2005) discuss the role of real radiative transfer in the accretion disc. The spin of the black hole is another physical parameter parameter to be considered Davis et al. (2005); Davis & Hubeny (2006). Qualitatively speaking, for the same black hole mass and accretion rate, these models push the peak of the SED to higher energies than due to the SS73 model. We would like to calculate line strengths corresponding to these models and test if the observations of BELs and NELs are sensitive enough to differentiate these accretion disk models from BBB.

• Comparison with data :
We intend to use the SDSS data base for Hβ 4861 Å, CIV 1549 Å and MgII 2798 Å and the HST and/or FUSE data base for OVI 1034 Å, to compare our predicted $\mathcal{EW}$ and line ratios with the observed line strengths. We would hope to draw constraints on other physical parameters (e.g. distance of the BELR) by such comparisons. Eventually we would want to extend our theoretical analysis to include other fundamental black hole parameters like the accretion rate. We would like to test if such systematic LOC modeling can explain observed effects like the "Balwin Effect" (Baldwin 1977), where the equivalent width of the CIV emission line decreases with increasing continuum luminosity.

• Narrow Emission Lines :
We intend to do similar studies for the NELs in the AGN spectrum. It would be interesting to see if they also show a mass dependence of the $\mathcal{EW}$, given that the NEL clouds are further away from the black hole and may be outside its sphere of influence (FWHM for NEL 1/6 of that for BELs) and/or their sizes are not governed by Keplerian dynamics.

5   CONCLUSIONS

• We wanted to investigate if there is a lower mass cut-off below which black holes cannot produce the broad emission lines (BELs) like Hβ 4861 Å, CIV 1549 Å and MgII 2798 Å typically used to detect and identify AGN activity from large optical data bases like the Sloan Digital Sky Survey.

• Using the standard LOC (locally optically emitting clouds) model for the broad emission line region (BELR) without any restrictions on the radius on its radius, photoionization calculations show an unobserved rise in the equivalent widths ($\mathcal{EW}$s) of the lines with decreasing mass.

• However, introducing a cut-off radius for the BELR produces sharp mass dependent drops in the $\mathcal{EW}$s, when the cut-off radius is determined from simple Keplerian mechanics, depending on the mass of the black hole (M_{BH}). Such drops are consistent with the observations including that below $M_{BH} = 10^5 M_\odot$ the above mentioned emission lines are not observed. Our findings conclude that these observations may not indicate the absence of black holes of such low mass, but the inability of such black holes to produce the observable (with our detectors) line strengths.

• Such a conclusion might have consequences for modifying the black hole mass function in the lower mass end. However, before we can attempt to address such issues, we need to carry out a more rigorous systematic study (listed above, in Section 4) of the $\mathcal{EW}$

of BELs and NELs, as a function of other fundamental black hole parameters like its accretion rate and alternative accretion theory models.

6 ACKNOWLEDGMENTS

REFERENCES

Allende Prieto, C., Lambert, D.L., & Asplund, M., 2001, ApJ, 556, L63

Allende Prieto, C., Lambert, D.L., & Asplund, M., 2002, ApJ, 573, L137

Arnaud, K. A. 1996, ASPC, 101, 17

Baldwin, J.; Ferland, G.; Korista, K.; Verner, D. 1995, ApJ, 455, L119

Baldwin, J. A. 1977, ApJ, 214, 679

Bentz, Misty C.; Peterson, Bradley M.; Pogge, Richard W.; Vestergaard, Marianne; Onken, Christopher A. 2006, ApJ, 644, 133

Binney J. & Tremaine S., 1987, "Galactic dynamic", Princeton, NJ, Princeton University Press.

Blaes, O.; Hubeny, I.; Agol, E. & Krolik, J.H. 2001, ApJ, 563, 560

Davis, S.W.; Blaes, O.M.; Hubeny, I. & Turner, N.J. 2005, ApJ, 621, 372

Davis, S.W. & Hubeny, I. 2006, ApJS, 164, 530

Ferland, G. J.; Korista, K. T.; Verner, D. A.; Ferguson, J. W.; Kingdon, J. B. & Verner, E. M., 1998, PASP, 110, 761-778

Frank, J.; King, A. & Raine, D.J. 2002, Accretion Power in Astrophysics, Cambridge Univ. Press, Cambridge.

Gezari, S.; Halpern, J. P.; Komossa, S.; Grupe, D.; Leighly, K. M. 2003, ApJ, 592, 42

Greene, J.E.; Ho, L.C. ApJ, 610, 722

Grevesse, N., & Sauval, A.J., 1998, Space Science Review, 85, 161

Hao, L. et al. 2005, ApJ, 129, 1783

Hills, J. G. 1975, Natur, 254, 295

Holweger, H., 2001, Joint SOHO/ACE workshop "Solar and Galactic Composition". Edited by Robert F. Wimmer-Schweingruber. Publisher: American Institute of Physics Conference proceedings, 598, 23

Hopkins, P. F.; Hickox, R.; Quataert, E.; Hernquist, L. 2009, MNRAS, 398, 333

Hubeny, I.; Agol, E.; Blaes, O. & Krolik, J.H. 2000, ApJ, 533, 710

Hubeny, I.; Blaes, O.; Krolik, J.H. & Agol, E. 2001, ApJ, 559, 680

Hui, Y.; Krolik, J.H. & Hubeny, I. 2005, ApJ, 625, 913

Kaspi, S.; Smith, P.S.; Netzer, H.; Maoz, D.; Jannuzi, B.T.; Giveon, U. 2000, AJ, 533 631

Korista, K.; Baldwin, J.; Ferland, G.; Verner, D. 1997, ApJS, 108, 401

Korista, K.; Ferland, G.; Baldwin, J., 1997, ApJ, 487, 555.

Leighly, K. M.; Casebeer, D. 2007, ASPC, 373, 365

Makishima, K.; Maejima, Y.; Mitsuda, K.; Bradt, H. V.; Remillard, R. A.; Tuohy, I. R.; Hoshi, R.; Nakagawa, M. 1986, ApJ, 308, 635

Mitsuda, K. et al. 1984, PASJ, 36, 741

Netzer, H. & Laor, A. 1993, ApJ, 404, L51

Netzer, H. 1987, MNRAS, 225, 55

Netzer, H.; Peterson, B. M. 1997, in Astronomical Time Series, eds., Maoz, D.; Sternberg, A.; Leibowitz, E. (Dordrecht: Kluwer), 85

Osterbrock, D.E. & Ferland, G.J. 2006, Astrophysics of gaseous nebulae and active galactic nuclei, University Science Press.

Peterson, B. M. 1993, PASP, 105, 207

Peterson, B. M. 1997, An Introduction to Active Galactic Nuclei, Cambridge Univ. Press, Cambridge.

Shakura, N. I.; Sunyaev, R. A. 1973, A&A, 24, 337

Stoughton, C. et al. 2002, AJ, 123, 485

Suganuma, M. et al. 2006, ApJ, 639, 46

Wright, E. L. 2006, PASP, 118, 1711